RSC Advances

PAPER

View Article Online
View Journal | View Issue

Cite this: *RSC Adv.*, 2025, **15**, 16540

BSA-ICG-Cu(II) complex as an NIR-responsive multifunctional platform for wound healing: deciphering therapeutic action *in vitro*†

Jayashree Roy,[a] Sahely Saha,[b] Manjari Shukla,[a] Sudipta Bhattacharyya,[a] Raviraj Vankayala[a] and Indranil Banerjee *[a]

Therapeutic platforms suitable for NIR-responsive antimicrobial treatments through photothermal and photodynamic modalities are gaining attention in treating chronic wounds. The efficiency of such platforms can be further enhanced by making them angiogenic and a promoter of fibroblast activities. Herein, we report a novel molecular platform composed of bovine serum albumin (BSA), indocyanine green (ICG) and bivalent copper (Cu(II)) using green chemistry by exploiting the affinity of ICG and Cu(II) ions towards BSA. We hypothesized that in the BSA-ICG-Cu(II) complex, ICG will help in producing heat and reactive oxygen species under NIR (808 nm) exposure, which can kill bacteria; Cu(II) will induce angiogenesis and BSA will activate dermal fibroblasts. The SEM images of the BSA-ICG-Cu(II) complex revealed a bead and fibril structure at the microscale. Biophysical studies (UV-vis-NIR, fluorescence and CD spectroscopy) indicated stable complex formation through the involvement of the hydrophobic BSA core. A study on NIR-mediated (808 nm LASER) killing of bacteria (*S. aureus* and *E. coli*) confirmed the photothermal and photodynamic efficiencies of the BSA-ICG-Cu(II) complex. At the cellular level, dermal fibroblasts, when treated with the BSA-ICG-Cu(II) complex, showed significant enhancement in cell migration and cellular VEGF expression (~2.8 fold). The *in vitro* angiogenesis study using HUVEC cells demonstrated that the complex can promote tube formation. In conclusion, the BSA-ICG-Cu(II) complex can serve as a multifunctional NIR-responsive therapeutic platform capable of exerting antibacterial, angiogenic and fibroblast-activating properties, which are beneficial for chronic wound therapy.

Received 7th January 2025
Accepted 17th April 2025

DOI: 10.1039/d5ra00155b

rsc.li/rsc-advances

1. Introduction

Phototherapy has gained attention as a potential modality to treat bacterial infection in chronic wounds.[1–4] Factors that provide an edge to phototherapy over conventional treatments are its minimal invasiveness, low toxicity, and drug-free broad-spectrum antibacterial effect.[5,6] Phototherapy refers to the application of light to achieve therapeutic benefits, primarily through photothermal and photodynamic modalities, often referred to as PTT and PDT, respectively. PTT uses photothermal materials to generate hyperthermia, *i.e.*, conversion of absorbed light energy into thermal energy, to kill bacteria. In contrast, PDT relies on the killing of bacteria by reactive radicals, especially, reactive oxygen species (ROS), produced by photosensitisers under irradiation.[7,8] Interestingly, it is often found that a single material/formulation can exhibit both photothermal and photodynamic properties when excited with light of an appropriate wavelength and confer exceptional antibacterial efficacy.[9–11] To date, there are several materials/formulations found to be responsive towards the wavelengths in the UV, visible, and near-infrared (NIR) regions and are explored for phototherapy applications.[12–17] In this regard, NIR-responsive phototherapy has started gaining momentum owing to its superior tissue penetration capabilities, reduced scattering, minimal autofluorescence, and relatively low tissue damaging properties.[1,18] NIR light (700–2500 nm) presents a broader wavelength range and less energy than the conventionally used visible and UV radiation.[19] Human tissues such as blood, skin, and fat tissues have shown negligible absorption and scattering coefficients in the NIR region.[20] Thus, NIR-light responsiveness can trigger localised treatments and imaging without damaging neighboring tissues.[21]

However, presently, there are only a few materials available that can be used as an NIR-responsive platform, such as copper ions-hydroxyapatite/polydopamine nanocomposites (HA-Cu/PDA), quaternized Cu-carbon dots (Cu-RCDs-C35), polypyrrole-bismuth oxychloride intercalated nanosheets (PPy-BiOCl) and indocyanine green (ICG).[22–24] Among these compounds, ICG is often preferred for its better performance and biocompatibility.

[a]*Department of Bioscience and Bioengineering, Indian Institute of Technology Jodhpur, Karwar 342030, India. E-mail: indranil@iitj.ac.in*

[b]*Technology Innovation and Startup Center (TISC), Indian Institute of Technology Jodhpur, Karwar 342030, India*

† Electronic supplementary information (ESI) available. See DOI: https://doi.org/10.1039/d5ra00155b

It has been experimentally proved that ICG confer therapeutic benefits by both PTT and PDT. Further, ICG is an FDA (Food and Drug Administration) approved dye for medical diagnosis and imaging applications. Several therapeutic formulations have been developed for anticancer therapy and wound healing applications with ICG.[25–29] However, the major drawbacks of ICG are its short plasma half-life and poor photostability in aqueous systems.[30,31] Moreover, ICG as a phototherapeutic agent can kill bacteria,[9,32] but to address other requirements of chronic wound healing, such as angiogenesis and dermal cell migration and differentiation, different research groups have tried to come up with several formulations[11,28,33–35] Most of these formulations encapsulated ICG into the bioactive or synthetic polymers, and metal–organic frameworks (MOFs), which involves complicated fabrication processes. Keeping these aspects in mind, in this study, we have developed a greener one-pot synthetic approach to prepare a novel multifunctional NIR-responsive molecular complex consisting of bovine serum albumin (BSA), ICG and Cu(II) ions for wound healing application. We hypothesised that in the molecular complex, ICG could act as an NIR (808 nm)-responsive phototherapeutic agent; (ii) Cu(II) ions will help in promoting angiogenesis; and (iii) BSA will work as a carrier for both ICG and Cu(II) ions, which will substantially enhance the photostability of ICG and will promote the cellular responses. The overall design and the possible functionality of the BSA-ICG-Cu(II) complex are shown in Scheme 1. Previously, it has been reported that the complexation of ICG with serum albumin can increase the photostability of ICG.[36] Further, the role of BSA as a drug carrier and modulator of cellular response in wound healing is already documented[37–39] and Cu(II) is known to promote angiogenesis by activating HIF-1α and subsequently enhancing cellular VEGF expression.[40–42] Finally, BSA can interact strongly with both ICG and Cu(II) in aqueous medium and BSA-Cu(II) often leads to stable insoluble precipitation. To test our hypothesis, we have developed the BSA-ICG-Cu(II) complex in Milli Q at 37 °C. The complex was subjected to thorough biophysical characterisation using UV-vis-NIR, CD and fluorescence spectroscopy. The microstructure of the complex was analysed using SEM. The complex photothermal and photodynamic properties in acellular conditions were checked and later employed to kill bacteria *in vitro*. The effect of the complex on angiogenesis and dermal fibroblast activities was also evaluated *in vitro*.

2. Materials and methods

2.1 Materials

Bovine serum albumin, heat shock fraction, protease-free, fatty acid-free, essentially globulin free, pH 7, ≥98% (Cat No. A7030), copper sulphate ($CuSO_4$, anhydrous powder, ≥99.99% trace metals basis, Cat No. 451657), 8-anilino-1-naphthalenesulfonic acid (ANS, Cat No. 10417), indocyanine green (ICG, Cat No. 21980), TRITC – phalloidin (Cat No. P1951) and 2′,7′-diacetyldichlorofluorescein (DCFH-DA, Cat No. D6883) were purchased from Sigma-Aldrich®. Calcein-AM (Cat No. TC474), Hoechst 33258 (Cat No. TC225), MTT reagent (3-(4,5-dimethylthiazol-2-yl)-2,5-diphenyltetrazolium bromide, Cat No. CCK003), Dulbecco's Phosphate Buffered Saline (DPBS) (Cat No. TL1006), dimethyl sulfoxide (DMSO) (Cat No. GRM5856), paraformaldehyde in PBS (Cat No. TCL119) and PVDF (polyvinylidene fluoride) syringe filters (0.22 μm) (Cat No. SF10) were purchased from Himedia. Propidium iodide (Cat No. 11195) from Sisco Research Laboratories (SRL). Dil stain (1,1′-dioctadecyl-3,3,3′,3′-tetramethylindocarbocyanine perchlorate ('DiI'; DiIC18(3))) (Cat No. D282) was purchased from Invitrogen. The EZXpand™ Human Umbilical Vein Endothelial Cell Culture Kit (Cat No. CCK026) and EZXpand™ Dermal Fibroblast Culture Kit (CCK027) were purchased from Himedia. Primary antibody of Smooth Muscle Actin (anti-mouse) (Cat No. sc-53142), and secondary antibody (Goat anti-Mouse IgG (H + L), FITC) (Cat No. 31569) were purchased from Santa cruz biotechnology and Invitrogen respectively. Luria Bertani Broth (Cat No: 14593) was purchased from Sisco Research Laboratories (SRL). Ultrapure Milli-Q water (18.2 MΩ) was used for the preparation. Bacterial strains *E. coli* DH5α and *S. aureus* RN4220 were obtained and used in Dr Sudipta Bhattacharya's laboratory at IIT Jodhpur.

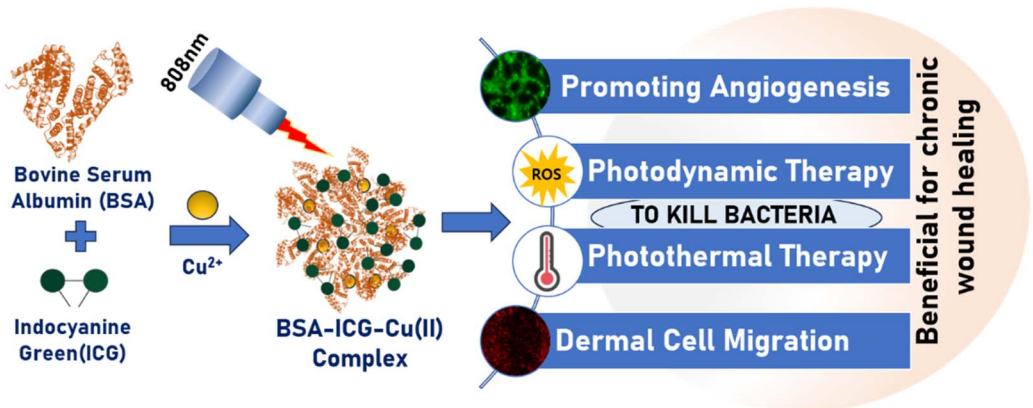

Scheme 1 Schematic representation of the overall design and activities of the BSA-ICG-Cu(II) complex as a multifunctional NIR-responsive therapeutic platform for addressing bacterial infection, angiogenesis and fibroblast activities.

2.2 One-step synthesis of the BSA-ICG-Cu(II) complex

For the synthesis of the BSA-ICG-Cu(II) complex, the BSA stock solution (0.2 mM), copper sulfate (10 mM) and ICG (645 μM) were prepared in milli Q water (18.2 MΩ). For the BSA-ICG-Cu(II) complex formation, 500 μl of BSA (0.2 mM), 155 μl of ICG (645 μM) and 60 μl of Cu(II) (10 mM) were mixed in a 1 : 1 : 6 molar ratio of BSA, ICG and Cu(II), respectively, and finally, the volume was made up to 1 ml with Milli Q water. The samples were then incubated for 1 h to study the precipitation process of BSA at 37 °C and then centrifuged to obtain the precipitate and washed with Milli Q two times to remove any free BSA and ICG in the formulation.

BSA-Cu(II) and BSA-ICG were also prepared for comparative analysis. For the preparation of BSA-Cu(II), 500 μl of BSA stock solution (0.2 mM) and 60 μl of Cu(II) from 10 mM stock prepared in Milli Q were mixed in 1 : 6 molar ratio to make up 1 ml of the solution. The sample was then incubated for 1 h for precipitation at 37 °C, centrifuged to obtain the precipitate and washed with Milli Q two times to remove any free BSA and Cu(II) in the formulation. For BSA-ICG complex formation, 500 μL of BSA (0.2 mM) and 155 μL of ICG (645 μM) were mixed and the volume was made up to 1 ml with Milli Q water and incubated at 37 °C for 1 h. All the experiments were done using freshly prepared samples. For physico-chemical analysis, further dilution was done using Milli Q whenever required.

2.3 Spectroscopic characterization of the BSA-ICG-Cu(II) complex

All the sample solutions were prepared in ultrapure Milli-Q water. The UV-vis-NIR spectrophotometer (Jasco V-770) was used to analyse the absorption spectra of free ICG, BSA, BSA-Cu(II), BSA-ICG, and BSA-ICG-Cu(II) for the wavelength range from 200 to 1100 nm taking Milli Q water as blank. A quartz cuvette with an optical path length of 3 cm was used.

The fluorescence emissions were recorded using a Jasco spectrofluorometer FP-8300 equipped with an Xe arc lamp (excitation source). The widths of both the excitation and emission slit were kept at 2.5 nm. Free BSA and BSA-containing samples (BSA-ICG, BSA-Cu(II) and BSA-ICG-Cu(II)) were excited at 280 nm, and emission was recorded from 300 nm to 500 nm to study the intrinsic fluorescence of the samples.

Further, the fluorescence emission was measured for the samples treated with 8-anilino-1-naphthalenesulfonic acid (ANS) at a photoexcitation wavelength of 380 nm, and the emission was recorded between 400 nm and 600 nm wavelength. For this experiment, the samples were incubated with ANS (10 μM) for one hour in the dark before the fluorescence measurements. All the samples were diluted 10-fold with Milli Q to make up the volume to 1 ml.

The 3D excitation–emission map for the sample was constructed by selecting an excitation wavelength range of 620–850 nm and an emission wavelength range of 635–895 nm with a 10 nm step size. The excitation and emission slit widths were at 5 nm and 10 nm, respectively. The spectra were plotted utilizing Origin software.

For the analysis of the secondary structure of the complex, circular dichroism spectroscopy was performed using Jasco J 815 Spectropolarimeter. At the far UV region (190 nm to 250 nm), the conformational changes of the protein samples were monitored. A concentration of 5 μM BSA was used for this experiment, and from BSA-ICG, BSA-Cu(II), and BSA-ICG-Cu(II) samples, 50 μl were taken and diluted to Milli Q to make up 1 ml of the final solution for analysis. Samples were taken in a cuvette of 1 mm of path length with a scanning speed of 50 nm min^{-1}.

2.4 Analysis of the micro-structure of the BSA-ICG-Cu(II) complex by scanning electron microscopy (SEM)

The morphology of the BSA-ICG-Cu(II) complex was analysed using a scanning electron microscope (SEM-EVO 18-Carl Zeiss). A lyophilized sample of BSA-ICG-Cu(II) was prepared for SEM imaging. The sample was then sputter coated with Au using a direct current sputter coater, and images were captured at 10 kV. The elemental mapping was done with EDAX (Oxford instruments, EDS-51-ADDD-0048, United Kingdom).

2.5 *In silico* study of the BSA-ICG-Cu(II) complex

The BSA and ICG were first simulated separately for 30 ns in an NPT environment to remove all the crystallographic and packing constraints. The ligand 2D structure was retrieved from the PubChem database (CID. 5282412) and converted into a 3D structure with Open Babel.[43] The protein crystal structure was downloaded from RCSB PDB (PDB Id. 4F5S)[44] with a resolution of 2.47 Å. The water and other non-bonded ligands were removed with PyMol. The simulation was carried out using a 10 Å cubic solvation box with dcd, xst, restart frequency 5000 while output energy was kept at 500. The timesteps were kept in 2 femtoseconds and 1 step per cycle. PME grid size x, y, z was kept at 100. The Langevin dynamics was used, and the temperature was set to 310 K. NAMD and VMD software were used for simulation. A molecular dynamics simulation study of the BSA ICG complex was performed to evaluate the stability of ICG with BSA in particular binding pockets under physiological simulated parameters. For the docking study, simulated BSA and ICG PDB files were taken as input files. Docking was done with AutoDock Tools 1.5.7 (ref. 45) with exhaustiveness 16 and the grid box was set for 1 Å spacing with grid sizes of x, y, and z 7.44, 25.33, and 117.90, respectively. All atomistic MD simulation experiments were conducted using the NAMD 2.14 (ref. 46) simulation platform. NAMD, a software for simulating molecular dynamics at the nanoscale, uses VMD[47] for preparing files. Utilizing the Charmm-Gui Ligand Reader and Modeller,[48] the ligands' trajectory and parameter files were obtained. Using Langevin dynamics, a solution cubic of 10 Å was established in the isothermal–isobaric ensemble (NPT) environment. In the conditions involving multiple time steps, time steps per cycle remained at 2 fs. At 5000, the dcd, xst, restart, and output energies were all configured. A 1000-step minimization process was conducted before the simulation and a 30 ns run was performed. After the simulation experiment, RMSD and RMSF files were generated with the VMD tool and assessed with Origin

software. Finally, the copper ions were docked with the BSA-ICG complex and six poses were analysed. (Kollman charges added, Polar hydrogens added, 1 Å spacing with grid size *x*, *y*, *z* 7.44, 25.33, 117.90).

2.6 Study of NIR-induced photothermal and photodynamic effects

Photothermal properties of the BSA-ICG-Cu(II) complex were determined by irradiating the sample with an 808 nm NIR laser at a power density of 0.33 W cm^{-2} for 5 minutes and subsequently measuring the temperature increase in the sample using a thermal camera (Model No. FLIR Cx-series). For this experiment, 300 μl of the sample (aqueous suspension of BSA-ICG-Cu(II) complex) was kept in a 1.5 ml microcentrifuge tube. The sample was then exposed to laser irradiation from the top of the tube with the lid open. The temperature increase was measured for 5 minutes at intervals of thirty seconds. The photostability of the complex under the 808 nm NIR excitation was checked for three ON/OFF cycles of 5 minutes duration of each phase at 0.3 W cm^{-2} laser power and temperature changes were recorded using the thermal camera. The NIR-induced ROS production from BSA-ICG-Cu(II) complexe was analysed by fluorimetry using a ROS-measuring dye DCFH-DA. For this purpose, sodium hydroxide (0.01 M) was first mixed with DCFH-DA (200 μM) in a 3 : 2 v/v ratio and incubated for 30 minutes at room temperature to facilitate the conversion of DCFH-DA to DCFH2.[49] The reaction was terminated by adding 3 ml of 0.1 M PBS. DCFH2 was then added to the sample suspension. The final concentration of the probe in the sample suspension was 5 μM. The samples were then irradiated with 808 nm CW laser at a power density of 0.3 W cm^2 for 5 minutes. After irradiation, the sample was excited at 405 nm and emission was recorded from 420–500 nm.

2.7 Study of NIR-mediated antimicrobial activity *in vitro*

We evaluated the antibacterial efficiency of the BSA-ICG-Cu(II) complex with and without NIR irradiation against *E. coli* DH5α (Gram-negative) and *S. aureus* RN4220 (Gram-positive). The glycerol-stored pure cultures that had been preserved earlier were used to perform quadrant-streak on the agar plate and thereafter incubated overnight at a temperature of 37 °C. Colonies collected from the fourth quadrant were then cultured for 24 h on a fresh nutrient agar plate using the quadrant-streaked method. For each bacterial strain, a single colony on a solid LB agar plate was dispersed in 5 ml of LB separately and cultured at 37 °C under shaking (110 rpm) until the optical density (OD@600 nm) of this suspension reached to 0.6 AU (arbitrary unit). 50 μL of log phase cultures of individual Gram-negative *E. coli* DH5α and Gram-positive *S. aureus* were added separately to a 96-well plate for different treatments. They were incubated with ICG (100 μL), BSA-ICG (100 μL), BSA-Cu(II) (100 μL) and BSA-ICG-Cu(II) (100 μL) for 2 h, separately. In the NIR groups, all samples were irradiated for 15 minutes (808 nm, 0.33 W cm^{-2}) in three cycles and cultivated in a bacterial incubator for a further 2 h. While in the non-NIR groups, the solutions were cultured in a bacterial incubator for 2 h without any further treatment. Post-incubation, the suspension was diluted 1000 folds and 50 μl of the diluted suspension was spread on the LB plate with a sterile spreader to cover the entire agar surface. Plates were incubated in a bacterial incubator for 24 h for bacterial colony formation. Post-incubation, images of the plates were taken and colony counting was done by image analysis using NIH-ImageJ software.

2.8 Evaluation of the effect of the BSA-ICG-Cu(II) complex on viability and functionality of human adult dermal fibroblast (HADF) cells

The effect of the BSA-ICG-Cu(II) complex on the viability and functionality of HADF was assessed *in vitro*. For all the cellular studies, the HADF cells were cultured in fibroblast-specific media at 37 °C in an incubator (5% CO_2 and 95% humidity). Prior to any assay, cells were harvested from the T25 flask by trypsinization. The effect of the BSA-ICG-Cu(II) complex on the viability of HADF cells was first qualitatively assessed through calcein AM staining. For this purpose, cells were seeded on the wells of a 96-well plate (10^4 cells per well) and incubated overnight to let them adhere to the surface of the plate. Subsequently, the cells were treated with 100 μl of the BSA-ICG-Cu(II) complex prepared in complete fibroblast media for 48 h. Post-incubation, cells were treated with Calcein-AM in PBS with the final concentrations of 2 μM and incubated at 37 °C for 30 min. The cells were then imaged using an Olympus IX73 fluorescence microscope.

The viability of the cells under the exposure of the complex was then checked using an MTT assay. For the MTT assay, cells were seeded in 96-well plates at a density of 10^4 cells per well and incubated overnight at 37 °C in an incubator (5% CO_2, 95% humidity). The cells were then treated with 100 μl of the BSA-ICG-Cu(II) complex prepared in complete media (complete fibroblast media) for 24 h. Post-treatment, 100 μl of the MTT reagent at a concentration of 0.5 mg ml^{-1} was added to the wells and the assay was performed as per the instructions provided with the kit. The absorbance was recorded at 570 nm using a microplate reader (Agilent EPOCH-SN). The experiment was done in triplicate and the cellular viability was calculated relative to that of the control. The statistical analysis was performed using one-way ANOVA for p-value < 0.05.

To quantify the cell death under the influence of the complex, flow cytometry was performed using PI. In 24-well plates, HADF cells were seeded (4×10^4 per well) and cultured in fibroblast-specific media. Cells were then treated with BSA-ICG-Cu(II) (13.5 mg ml^{-1}) for 24 h. Post-treatment, cells (in the supernatant and adhered) were collected together and centrifuged at 1000 g for 5 minutes to form a pellet. It was then washed with PBS and resuspended in PBS. After that, the cell suspension was treated with a PI solution (final concentration of 50 μg ml^{-1}) for 15 minutes at room temperature in the dark. The total cell population was then examined using a flow cytometer (FACS Accuri C6, BD Biosciences).

The effect of the complex on the cytoskeletal organization was studied by immunocytochemistry using phalloidin-TRITC as an F-actin specific probe. For this study, cells were treated

with the BSA-ICG-Cu(II) complex for 24 hours. After incubation, the cells were fixed with a 4% paraformaldehyde solution in PBS to fix them and then stained with TRITC (tetramethyl rhodamine isothiocyanate)-phalloidin and Hoechst. The imaging was done using a fluorescence microscope (Olympus IX73) equipped with a CMOS camera.

Migration of the HADF cells under the influence of the complex was measured by a scratch assay. For this purpose, HADF cells were stained with membrane-binding vital dye DIL. The Dil-stained cells were then seeded in the wells of a 24-well plate at a density of 4×10^5 cells per well and cells were incubated for 48 h to reach confluence. After that, a sharp scratch was made through the confluent layer using a 10 μl-micropipette tip. After making the scratch, the old media was removed, and fresh media containing the complex was added to the well. Cells treated with only media (without complex) were taken as control. Covering of the scratch due to cell migration was then visualized using a fluorescence microscope.

To study the effect of the complex on the differentiation of HADF, cells were incubated with 13.5 mg ml^{-1} of sample for 7 days. Post-incubation, cells were fixed with 4% paraformaldehyde, permeabilised with 01% Triton X, blocked with 5% BSA and probed with the primary antibody against α-SMA (1 : 500) and the corresponding FITC-conjugated secondary antibody (1 : 500). The immune-stained cells were counterstained with Hoechst. Imaging was done using a fluorescence microscope.

The effect of the BSA-ICG-Cu(II) complex on the cellular expression of VEGF in HADF was analysed using a Human VEGF ELISA kit (Abcam 100662). In brief, 3×10^4 HADF cells were seeded in each well of a 24-well plate and allowed to adhere for 24 h in a cell culture incubator. The cells were then treated with BSA-ICG-Cu(II) for 24 h. Post-treatment, the supernatant was collected and added to the wells of the pre-coated ELISA plate. The ELISA procedure was conducted following the protocol provided by the Company (Abcam), and absorbance was recorded at 450 nm.

2.9 Study of BSA-ICG-Cu(II) induced angiogenesis *in vitro* (HUVEC cell tube-forming assay)

To evaluate the angiogenic property of the complex *in vitro*, a tube formation assay was performed using HUVEC cells. HUVEC cells were cultured in a gelatin-coated T-25 flask in HiEndoXL Endothelial basal medium (part B) supplemented with endothelial cell growth supplement (part C) in a cell culture incubator (95% humidity, 5% CO_2 at 37 °C) as per the protocol provided by the supplier of the cell (Himedia). For the tube formation assay, fibrin gel from CELLINK was added to a 96-well tissue culture plate (50 μL per well). The bed was cured with 365 nm UV light for 40 seconds, after which 1×10^4 HUVECs were seeded per well. The cells were treated with BSA-ICG-Cu(II), and the control group was given complete endothelial media. The cells were incubated at 37 °C for 12 h and the development of angiogenic networking (tube formation) was evaluated using calcein-AM staining. Representative pictures of tube formation were taken at 10× magnification with a fluorescence microscope with z-stacking (Olympus, USA). Further, quantification of the tubular network formation was done by image analysis using the NIH ImageJ software, angiogenesis plug-in to check the number of Meshes, Junctions, Branches, and Master Segments.

2.10 Statistical analysis

The experiments were done in triplicate, and data were expressed as mean ± SD. Statistical significance was assessed by one-way ANOVA. '*P*' Value less than 0.05 was considered significant.

3. Results and discussion

3.1 Synthesis and characterization of the BSA-ICG-Cu(II) complex

ICG has a high affinity for BSA and binds to the hydrophobic pockets of albumin.[29,50,51] On the other hand, copper ions (Cu(II)) can bind with BSA to form an insoluble precipitate at various stoichiometries.[40,51,52] Here, we exploited the aforementioned properties of BSA, ICG and Cu(II) ions to develop the proposed BSA-ICG-Cu(II) complex. We observed that the formation of the BSA-ICG-Cu(II) complex results in a dense, visible green precipitate (high turbidity) at 37 °C in water within a few seconds after the addition of Cu(II) and ICG into BSA solution [see the inset in Fig. 1A]. The UV-vis-NIR absorption spectra of BSA-ICG-Cu(II) are shown in Fig. 1A. Analysis of the spectra revealed that, for the BSA-ICG-Cu(II) complex, the characteristic peaks of BSA at 278 nm,[53,54] which arise due to the presence of tryptophan, tyrosine, and phenylalanine are partly masked.[55,56] Similar masking was observed in the case of BSA-Cu(II) but not for BSA-ICG. Therefore, it may be assumed that such masking is probably because of the interaction of Cu(II) ions with the aromatic amino acids in BSA. On the other hand, the free ICG gives characteristic absorption peaks at 713 nm and 780 nm. With the addition of ICG to BSA, there is an increase in the overall absorbance, as well as a significant red shift in the absorption of the peak from 713 nm to 734 nm (~21 nm), and for the monomeric peak, from 780 nm to 804 nm (~24 nm), respectively. A similar redshift was also observed for BSA-ICG-Cu(II), indicating a strong interaction between the BSA and ICG molecules.[57] CD spectroscopy (Fig. 1B) showed drastic dissimilarities between the spectra of BSA and BSA-ICG-Cu(II), indicating a structural change in the secondary structure, especially the native α-helical structure of BSA.[58] Interestingly, the CD spectrum of BSA-ICG was found to be similar to that of BSA, which implies that the binding of ICG to BSA has minimal effect on the secondary structure of BSA. On the contrary, the CD spectrum of BSA-Cu(II) was found analogous to BSA-ICG-Cu(II), indicating that the structural changes in the protein were due to its interaction with Cu(II). The fluorescence emission spectra of the samples were recorded by photoexcitation at a 280 nm wavelength, and the emission data were collected from 300 nm to 500 nm (Fig. 1C). BSA generates a strong fluorescence emission peak at 337–340 nm at 280 nm excitation.[59] We observed a reduction in the intrinsic fluorescence intensity of BSA

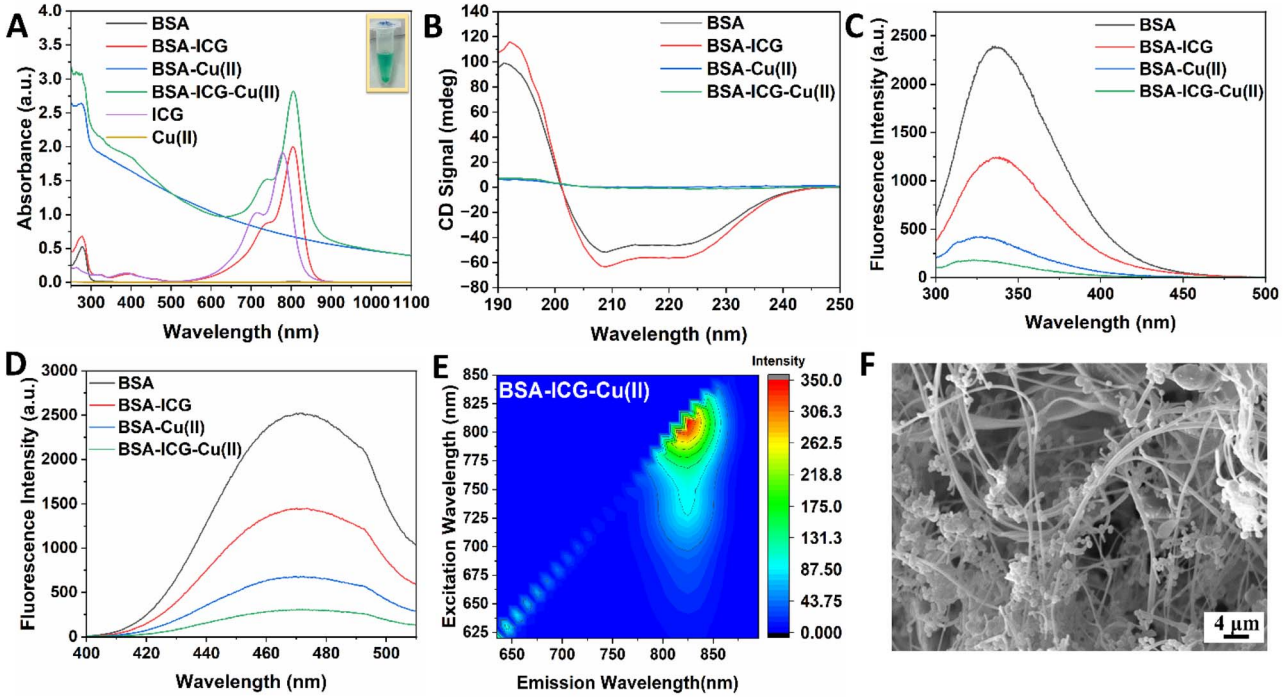

Fig. 1 Biophysical characterization of the BSA-ICG-Cu(II) ion complex: (A) UV-vis-NIR spectra [inset: BSA-ICG-Cu(II) complex], (B) secondary structural analysis using circular dichroism spectroscopy. (C) Intrinsic fluorescence emission spectra recorded at $\lambda_{ex} = 280$ nm and $\lambda_{em} = 300–500$ nm, (D) 8-aniline-1-naphthalene sulfonic acid (ANS) fluorescence spectra at $\lambda_{ex} = 380$ nm and $\lambda_{em} = 400–600$ nm. (E) Excitation–emission (EEM) mapping and (F) scanning electron microscopy images of lyophilized BSA-ICG-Cu(II). All the spectra were recorded in Milli-Q at RT.

following the addition of ICG. Likewise, the introduction of Cu(II) ions to BSA also diminished the emission intensity. Such a decrease in the emission intensity was found to be maximum for the BSA-ICG-Cu(II) complex. Previously, it was reported that such type of fluorescence quenching often implies the structural alterations in BSA resulting from the interaction of albumin fluorophores (aromatic amino acids) and the quencher.[60,61] Fig. 1D indicates the change in the hydrophobicity of BSA when the ICG and Cu(II) ions interact with it. The fluorescence intensity of ANS was evaluated to assess the accessibility of the hydrophobic areas in the protein. ANS is an extrinsic fluorophore that exhibits modest fluorescence when it binds with the hydrophilic domain of the protein but demonstrates high fluorescence when exposed to a hydrophobic environment.[62] Probing with ANS revealed that there is a decrease in ANS fluorescence from BSA after the addition of ICG and Cu(II). The BSA-ICG-Cu(II) complex had the lowest and most substantial quenching. This may happened because of the lower accessibility of ANS to the hydrophobic core of BSA due to structural changes in BSA after interaction with ICG and Cu(II). Considering this finding along with the observation of the intrinsic fluorescence study, it can be inferred that BSA has a strong interaction with ICG and Cu(II) that leads to the change in protein structure. An excitation–emission mapping (EEM) is a three-dimensional fluorescence scan indicating the correlation between excitation and emission wavelengths, generating a contour plot illustrating fluorescence intensity for each wavelength pair. This approach yields extensive spectrum data, facilitating an in-depth investigation of fluorophores and their interactions within a sample.[63] Fig. 1E illustrates the three-dimensional excitation–emission mapping of the BSA-ICG-Cu(II) complex. The excitation range was noted to be between 780–820 nm, with an emission hotspot occurring at approximately 820–835 nm. In contrast, for free ICG, the excitation wavelength ranges between 768–785 nm, and the emission hot spot was found at 795–810 nm (data not shown). This fact indicates a clear redshift in the fluorescence emission of the BSA-ICG-Cu(II) complex when compared to that of free ICG. Further, the SEM analysis of the morphology of the BSA-ICG-Cu(II) complex showed the formation of a mesh-like structure composed of randomly distributed fibrillar threads and beads in the micrometer range (Fig. 1F). The average bead diameter was found to be 1–3 μm, whereas the fibril diameter was in the range of 0.6–1 μm. This structure was distinctly different with respect to BSA, BSA-ICG, and BSA-Cu(II) (Fig. S1†). An EDAX analysis showed that Cu(II) is present in both beads as well as in fibrils (Fig. S2†). This type of structure is not very common in the literature. A structure partly resembling the findings was earlier reported by Kida *et al.* for human serum albumin-based formulations.[64] The presence of a broad halo and the absence of any distinct peak in the XRD profile (Fig. S3A†) indicates the amorphous nature of the complex. The existence of copper in the +2 valence state in the complex was confirmed by the potassium ferrocyanide test (Fig.S3B†). Further, the ICP-OES analysis revealed that the quantity of the Cu was 5.3 μg mg^{-1} of the complex.

3.2 *In silico* study of the BSA-ICG-Cu(II) complex formation

It is already reported that a wide variety of drug molecules can bind to serum albumin.[65] Such interactions between BSA and drug molecules have often been checked *in silico* through molecular docking studies to gain insight into the binding site and energy. Here, we have performed the *in silico* study to elucidate the binding of ICG and Cu(II) with the BSA and its impact on the overall structure of the BSA. To mimic the physiologically relevant ligand–protein interactions, the in-solution conformations of the interacting ligands and the receptor protein were simulated before the docking. Intriguingly, the docking results suggest the receptor protein BSA binds with ICG with a high free energy of binding (ΔG binding) of ~ -8.6 kcal mol^{-1}. Importantly, ICG was found to dock at the domain IIA of BSA, which is also known as Sudlow site 1 (Fig. 2A). This binding site is also referred to as drug binding site 1 and is also known to bind other clinically used drugs like warfarin, Indomethacin[66] *etc.* Importantly, the docked conformation of ICG at Sudlow site 1 is found to be principally stabilized by an array of hydrophobic interactions, which also corroborate its excellent free energy of binding (-8.6 kcal mol^{-1}) (Fig. 2B and C). Moreover, the atomistic MD simulation-mediated in-solution stability analysis of the free-floating and BSA-bound ICG molecule indicates the greater stability of the molecule in the BSA-bound state during the simulation time trajectory of 30 ns (Fig. 2D). The docked conformation of the ICG molecule showed the proximity of the sulfonic acid group of docked ICG to the Trp213 of BSA (Fig. 2B and C), which is well-aligned with the quenching of intrinsic fluorescence as reported in the previous section. A further docking study of copper (up to 6 Cu(II) binding) with the BSA-ICG complex gives us the probable binding sites of copper (Fig. 2E and F) with corresponding free energy of binding (ΔG binding) values ranging from -1.2 to -1.0 kcal mol^{-1} (Fig. 2G). The first copper ion (Cu-I) was found to bind mainly at the N-terminal site (NTS) of BSA (domain IA, IB) and domain IIA, which was previously proved to be metal binding site (MBS) adjacent to drug binding site 1 and is the most explored metal

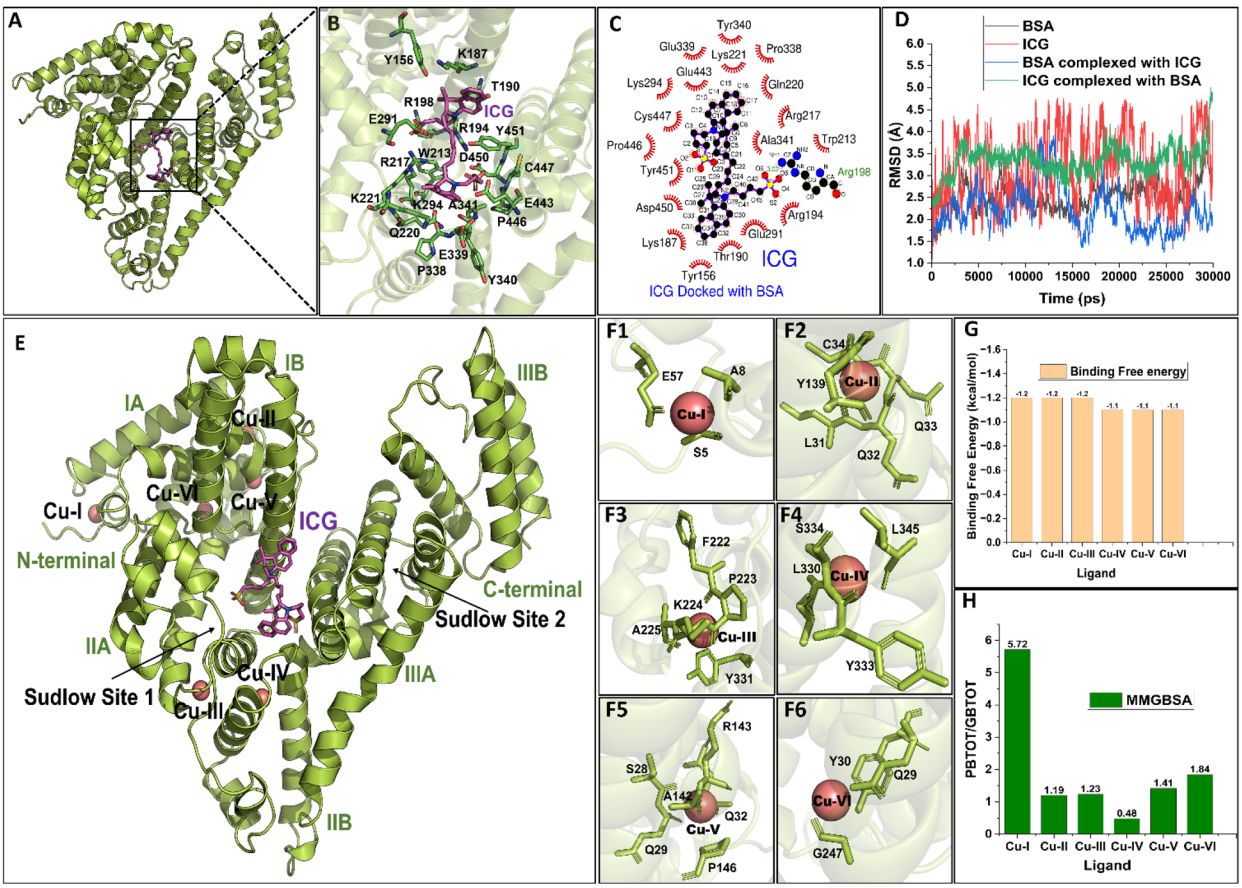

Fig. 2 *In silico* studies of interaction of BSA, ICG and copper ions: (A and B) snapshot represents the binding site of ICG (stick representation in magenta) with BSA (cartoon representation in green), which is at drug binding site 1 (Sudlow site 1) and three-dimensional orientation of the interacting residues of BSA with ICG at the binding site. (C) Two-dimensional interaction profile of ICG with active site amino acid residues (red spiked arch shows hydrophobic interaction between amino acids and ICG; green dotted line represents the hydrogen bond formed between the amino acid residue and ICG). (D) Comparative RMSD time trajectories of ICG in an unbound form *versus* ICG bound to BSA and BSA alone calculated through all-atomistic molecular dynamics simulation analysis. (E) Snapshots of the putative binding sites of six copper ions with BSA in the presence of docked ICG, (F1–F6) 3D representation of the BSA amino acid residues interacting with docked copper ions. (G) Free energy of binding of copper ions at different putative BSA interaction sites, and (H) MMGBSA values corresponding to six different putative copper-binding sites of BSA.

binding site of albumin (Fig. 2E and F1). Copper-II (Cu-II) interacts with free Cys-34 in the pocket of domain IA, which has been proven to be a metal binding site for metals, which makes a single metal sulfur bond[67] (Fig. 2F2). Cu-III and Cu-IV bind at the multi-metal binding site (MBS)[68] (Fig. 2F3 and F4). Earlier biochemical studies support the binding sites of copper, mainly in NTS and MBS.[67]

The free energy of binding of Cu(II) ions with BSA has also been rescored with the molecular mechanics generalized Born surface area (MMGBSA) method to improve the post-docking binding free energy calculation performed with AutoDock scoring function and from this analysis, we found that Cu-I has the highest free energy of binding and should be the most favored copper-binding site of BSA (Fig. 2H). Overall, the simulation results were matching with the findings of biophysical characterization, especially with intrinsic fluorescence data. The binding of copper(II) with BSA-ICG was experimentally confirmed by treating the BSA-ICG-Cu(II) complex with EDTA of varying concentrations (0.1 mM^{-1} mM^{-1}) and obtaining the subsequent UV spectra (Fig. S4†). It was found that with an increase in the EDTA concentration, the UV spectrum of BSA-ICG-Cu(II) changes to the characteristic UV spectrum of BSA-ICG (Fig. 1A). Such changes happened because of the removal of Cu(II) from the complex by EDTA (chelator), leading to the restoration of the 278 nm peak in the EDTA-treated BSA-ICG-Cu(II) complex. It also suggests the association of Cu(II) to the near vicinity of the tyrosine/tryptophan residue in the complex found in simulation data (Fig. 2F1–F6).

3.3 Study of NIR-induced photothermal and photodynamic effect

ICG showed both photothermal and photodynamic activities when activated by an 808 nm NIR laser. A part of the incident NIR light energy gets absorbed by the ICG and converts the energy into heat *via* photothermal processes,[69] while photodynamic activation of ICG creates singlet oxygen and other oxygen-containing free radicals. Here, we observed that at 0.3 W cm^{-2} NIR exposure for 5 min, the change in the temperature (ΔT) for the BSA-ICG-Cu(II) is 12 °C, whereas the same for BSA-ICG and ICG were 20.1 °C and 19.1 °C, respectively (Fig. 3A). This suggests that just like BSA-ICG, BSA-ICG-Cu(II) can also be used as an agent for NIR-induced mild hyperthermia, a technology now considered to be an effective methodology for wound healing. It is now proven that mild hyperthermia can cause bacterial killing along with the promotion of angiogenesis, cellular proliferation and tissue repair.[70–72] We also observed that at 0.3 W cm^{-2} NIR exposure, the rate of the change in temperature is more gradual for BSA-ICG-Cu(II) than BSA-ICG, which offers better control over the process for further therapeutic applications. The temperature rise for control (Milli Q) and BSA-Cu(II) was found to be negligible under the same experimental condition. The photothermal efficiency of the BSA-ICG-Cu(II) complex was found to be 46.5%. After confirming the photothermal properties of BSA-ICG-Cu(II), its photostability was further checked for 3 cycles (Fig. 3B). The BSA-ICG-Cu(II) complex was found to be photostable till 3 cycles. Subsequently, the photodynamic properties, *i.e.*, the capacity to generate ROS by the BSA-ICG-Cu(II) complex under NIR exposure, were further checked using DCFH-DA.[73] ROS produced by the samples under NIR exposure (as measured by DCF fluorescence intensity) was found to be the highest for the BSA-ICG-Cu(II) complex, which is ~10-fold higher than that of the control (Fig. 3C). The same for BSA-ICG was only ~3-fold. This data implied the strong photodynamic property of the BSA-ICG-Cu(II) complex.

3.4 Study of NIR-mediated antimicrobial activity *in vitro*

Antimicrobial phototherapy is generally achieved using photothermal and/or photodynamic agents.[74] ICG, as well as BSA-ICG, has so far been explored for phototherapy in cancer.[36] ICG has also been used in various nanoformulations for the phototherapy of wounds.[32,34,75] However, one of the critical issues in photothermal therapy (part of phototherapy) regarding the treatment of bacteria-infected wounds is the thermal injury at the tissue site due to overheating. To avoid this problem, researchers have used the 808 nm NIR laser at a power density of 0.3 W cm^{-2}. It is observed that such practice leads to minimal or no damage to the wound tissue.[76–78] At this laser exposure, temperature generally rises 40–50 °C, and the condition is often reported as mild hyperthermia[72,79,80] It is reported that mild hyperthermia not only contributes to bacterial killing but also improves the other components of healing response like angiogenesis and cellular proliferation as mentioned in the earlier section. Keeping the abovementioned perspective in mind, here, we have checked the efficiency of the BSA-ICG-Cu(II) complex as an NIR-responsive phototherapeutic antibacterial agent under 808 nm NIR exposure at 0.3 W cm^{-2} power density. We observed that the BSA-ICG-Cu(II) complex could efficiently reduce the bacterial load for both *S. aureus* (Gram-positive) and E. coli DH5 alpha (Gram-negative), as evidenced in Fig. 4A and B, respectively. Quantitative analysis in terms of colony counting revealed that for the BSA-ICG-Cu(II) complex, there was more than a 95% reduction in colony count (Fig. 4C and D). The same was also found true for BSA-ICG. Earlier, similar efficacy was reported for BSA-ICG and Bacitracin-Engineered BSA/ICG nanocomplex but with the use of higher laser power density.[32] It has to be noted that the usage of high 808 nm NIR laser power intensities might vary the contributions of both hyperthermia and photodynamic ROS generation. This highly promising result at 0.3 W cm^{-2} power density can be correlated to the mild hyperthermia and ROS generation capacity of the complex, as reported in section 3.3. One important finding of the study is that even without NIR light irradiation, the BSA-ICG-Cu(II) complex kills almost 60% of the bacteria. This may be because of the generation of more ROS by the Fenton-like reaction between Cu^{+2} ions and H_2O_2 generated by ICG. This indicates an inherent antimicrobial property of the BSA-ICG-Cu(II) complex[81,82]

3.5 Study of the effect of the BSA-ICG-Cu(II) complex on the viability and functionality of HADF cells

Indocyanine green (ICG) and bovine serum albumin (BSA) are both biocompatible and often used in various formulations, as they are approved by the USFDA.[83] On the other hand, copper

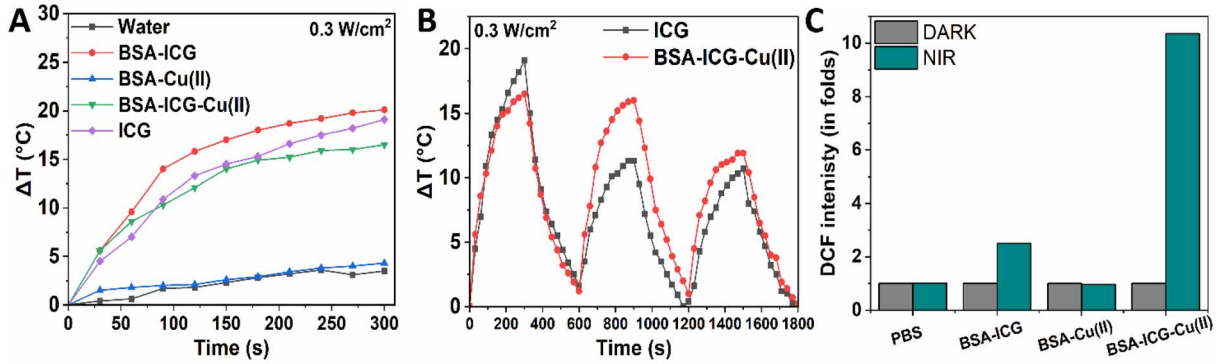

Fig. 3 Photothermal and photodynamic properties of the BSA-ICG-Cu(II) complex: (A) photothermal temperature rise when samples are irradiated for 5 min with an 808 nm CW laser at 0.3 W cm^{-2} power density. (B) Photothermal stability of BSA-ICG-Cu(II) and free ICG in Milli Q exposed to laser (0.3 W cm^{-2}) for three cycles of 5 min ON and 5 min. (C) Acellular ROS generation using DCFHDA. All the measurements were recorded in deionized water.

plays a crucial role in different cellular processes in living species, including humans.[84] It is reported that copper promotes the proliferation of dermal fibroblasts and facilitates wound healing by promoting angiogenesis and new ECM synthesis.[85,86] Thus, from the individual component's perspective, BSA, ICG and Cu(II) are all suitable for biological applications. However, the effect of the BSA-ICG-Cu(II) complex on the viability and functionality of HADF needs to be examined to propose its application for wound healing. Here, we first assessed the viability of HADF *in vitro* under the treatment of BSA-ICG-Cu(II) qualitatively by calcein-AM staining (Fig. 5A1 and A2)). Calcein AM is a vital dye that enters live cells due to its lipophilic nature, where intracellular esterase cleaves it, liberating calcein, which provides green fluorescence under appropriate excitation and thus provides information about cell viability and dynamics.[87] The fluorescent images suggest that BSA-ICG-Cu(II) has no detrimental effect on cell viability. The effect of the complex on HADF was further evaluated quantitatively by MTT assay and flow cytometry. Based on the MTT data obtained in our studies, it is clear that BSA-ICG, BSA-Cu(II), and BSA-ICG-Cu(II) samples

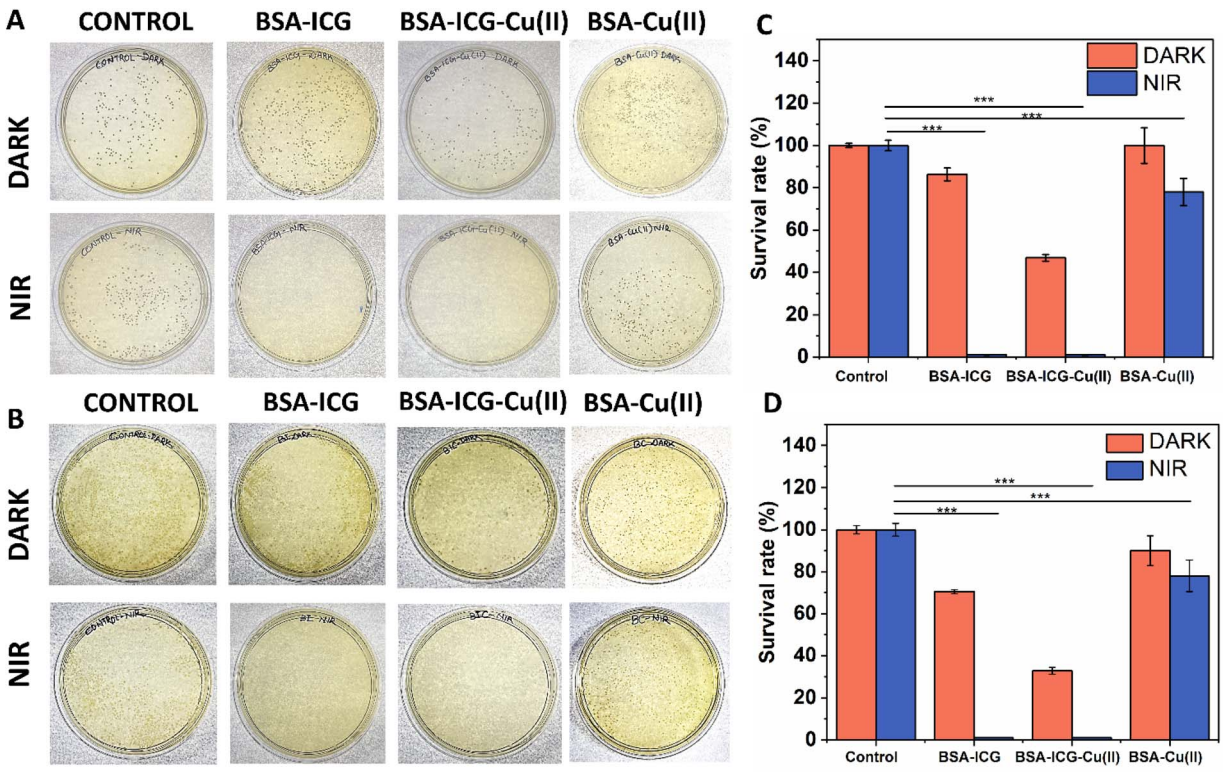

Fig. 4 Bacterial colonies formed by (A) *S. aureus* and (B) *E. coli* after treatment with BSA-ICG, BSA-Cu(II) and BSA-ICG-Cu(II) with or without NIR (808 nm, 0.3 W cm^{-2}). The survival rate of (C) *S. aureus* and (D) *E. coli* after treatment was determined using the plate counting method. Mean ± SD ($n = 3$); for the analysis of statistical significance, p value was found <0.001.

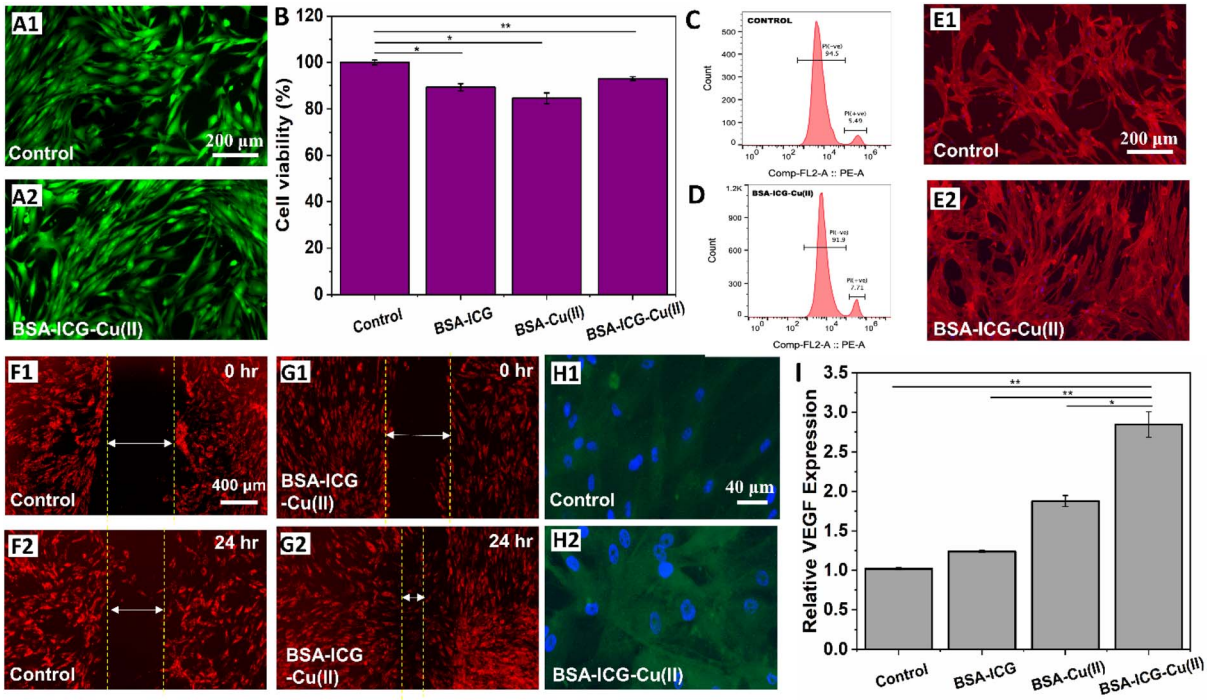

Fig. 5 Assessment of the cytocompatibility on HADF cells. (A1 and A2) Study of the viability of HADF cells by calcein-AM. (B) Study of the cell viability by the MTT assay. (C and D) Analysis of dead cell population through flow cytometry using propidium iodide (PI) to evaluate dead cells. (E1 and E2) Study of the cytoskeletal organization by F-actin staining using TRITC-phalloidin. (F–G) cell migration assay. (F1 and F2) Control and (G1 and G2) BSA-ICG-Cu(II) post-24-hours. Cells were stained with a vital dye DIL. The images were taken with a 4× objective and the scale bar corresponds to 400 μm. (H) Study of the expression of α-SMA by HADF (green colour). Nucleus was counterstained with Hoechst stain (blue). The images were taken with a 40× objective and the scale bar corresponds to 40 μm. (I) Study of the expression of cellular VEGF by the HADF using ELISA. Data reported: Mean ± SD ($n = 3$); for the analysis of statistical significance, p value was taken as <0.05.

have minimal cytotoxic effects (Fig. 5B). The MTT result indicates that the BSA-ICG-Cu(II) complex is compatible with the HADF cell and thus can further be explored for the preparation of wound healing formulation. The biocompatibility of BSA-ICG-Cu(II) could be ascribed to the intrinsic biocompatibility of ICG and BSA and copper(II) (Cu(II) at low concentrations).[72] Analysis of the dead cell population by flow cytometry using PI further confirmed the findings of the Calcein-AM and MTT study (Fig. 5C and D). For both the control and BSA-ICG-Cu(II) treated cells, the dead cell population was found to be less than 10%, *i.e.*, viability >90%. The physiological condition of adherent cells under the treatment of the BSA-ICG-Cu(II) complex was also assessed by analysing cytoskeletal organization. As seen in Fig. 5E1 and E2, the cells appeared properly adhered with characteristic adherent morphology. Actin filaments were formed across the cells in the BSA-ICG-Cu(II) complex, similar to those found in the control cells. For all samples, *i.e.*, BSA-ICG, BSA-Cu(II), and BSA-ICG-Cu(II), no spherical cells or cell aggregates were observed. It was found that the complex has no detrimental effect on the cytoskeletal organization.

Migration of dermal fibroblasts is an essential component of wound healing.[88] Commonly, to analyse the fibroblast migration, *in vitro* scratch assay is performed.[89] BSA and Cu(II) are reported to have a positive effect on fibroblast migration;[86] however, no comprehensive data is available for ICG alone. Here, to evaluate the effect of the complex on dermal cell migration, we performed a scratch assay, and images were acquired at 0 h and 24 h after the treatment. During the wound healing assay, the BSA-ICG-Cu(II) complex-treated cells filled the scratch area much faster than untreated control cells (Fig. 5F1, F2, G1 and G2). The result suggests that the complex enhances the migration of HADF cells in comparison to the control. To assess the effect of the complex on converting the fibroblast to the contracting subtype (myofibroblast), the expression level of alpha-smooth muscle actin (α-SMA), a positive marker of myofibroblast was checked qualitatively by immunocytochemistry. We observed a higher expression of α-SMA in the BSA-ICG-Cu(II) treated fibroblasts compared to the control (Fig. 5H1 and H2). Keeping the healing of chronic wounds in mind, we further checked the influence of the complex on cellular expression VEGF by HADF since VEGF plays a significant role in activating endothelial cells and subsequently promoting angiogenesis.[90] F Shams *et al.* reported that fibroblast cells expressing VEGF are accountable for enhanced numbers of blood vessels, accelerating angiogenesis in the wound healing process and improving wound healing.[91] In this study, BSA-ICG-Cu(II) showed the highest VEGF expression of 3-fold in comparison to the TCP (Fig. 5I). Among all the samples, BSA-ICG-Cu(II) induced the highest expression (2-3-fold increase), followed by BSA-Cu(II) (1-fold increase). BSA-ICG showed the least expression of VEGF, which was almost equivalent to the control. This data implied that the presence of Cu(II) in formulation for HADF directly

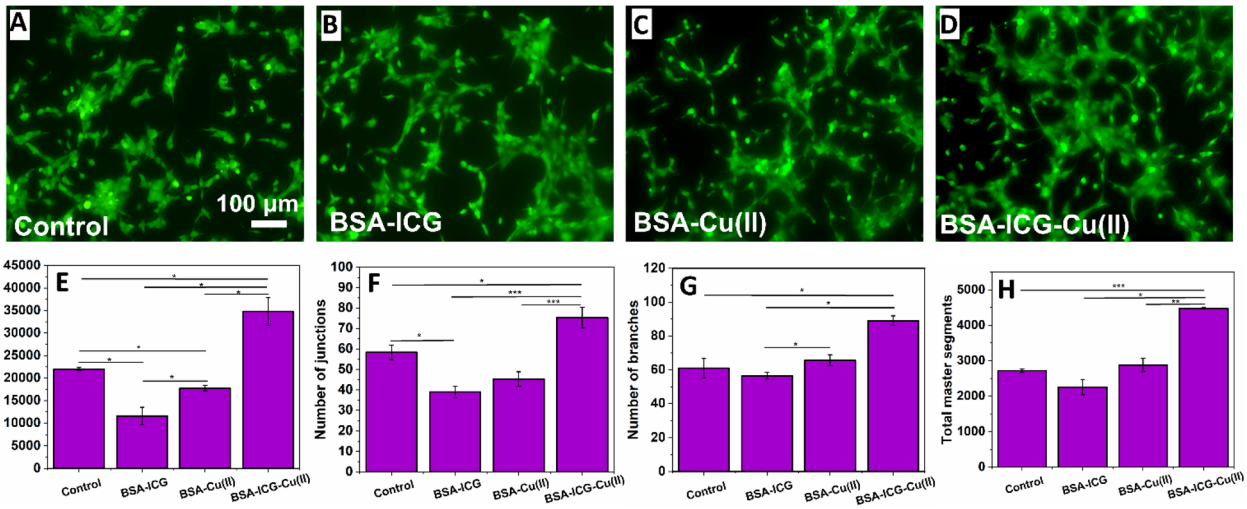

Fig. 6 (A–D) Comparative analysis of the angiogenic properties of the BSA-ICG-Cu(II) by the HUVEC tube formation assay. Cells were stained with the vital fluorescence dye calcein-AM (green). Calculation of the (E) No. of junctions, (F) No. of branches, (G) No. of junctions, and (H) total master segments *via* image analysis using NIH ImageJ software with an angiogenesis plug-in. Data reported: mean ± SD ($n = 3$), $p < 0.05$.

influenced the VEGF synthesis. The promoting effect of Cu(II) ions on angiogenesis is well-agreed. Cu(II) has been shown to activate angiogenic growth factors such as VEGF and FGF (fibroblast growth factor) due to activation of hypoxia-VEGF secretion, MAPK, and tyrosine kinase pathways.[40] In the skin, copper stimulates dermal fibroblast proliferation[92] Copper is also required for the activation of hypoxia-inducible factor-1 (HIF-1), a major transcription factor regulating the expression of VEGF.[93] Considering the effect of BSA-ICG-Cu(II) on the HADF cells (viability, cytoskeletal organization, migration, differentiation, and VEGF expression), it can be inferred that the complex acts as a promoter of the dermal fibroblast activities essential for chronic wound healing.

3.6 Effect of the BSA-ICG-Cu(II) complex on angiogenesis (study of *in vitro* tube formation assay in HUVEC cells)

Angiogenesis plays a key role in wound healing, involving migration and proliferation of endothelial cells.[94] Restoring blood flow to the site of chronic wound tissue is a prerequisite for mounting a successful repair response. In this study, we evaluate the angiogenic potential of the BSA-ICG-Cu(II) sample by *in vitro* tube formation assay using HUVEC cells (Fig. 6A–D). From the image, it is evident that BSA-ICG-Cu(II) promotes the formation of a tubular network among HUVEC cells. A similar network structure was observed in BSA-Cu(II) but not in the case of BSA-ICG. This has also been verified by image analysis using the NIH-ImageJ software with an angiogenesis plug-in. For a quantitative understanding of the tube formation assay, the numbers of meshes, junctions, segments, and relative tube lengths were measured. In the four groups, including the control, BSA-ICG, BSA-Cu(II), and BSA-ICG-Cu(II), we observed that all the aforesaid parameters were the highest for the BSA-ICG-Cu(II) group [Fig. 6E–H]. For the control, BSA-ICG, BSA-Cu(II) and BSA-ICG-Cu(II), the total number of meshes were 21991 ± 330, 11570 ± 1957, 17774 ± 609 and 34788 ± 3070; numbers of junctions were 58.33 ± 3.51, 39 ± 2.82, 45.33 ± 3.51 and 75.33 ± 5; the number of branches was 61 ± 5.65, 56.5 ± 2.12, 65.66 ± 3.21 and 89 ± 2.82, and the total master segments were 2720.5 ± 53.03, 225 ± 564.27, 2877.5 ± 190.21 and 4477 ± 2.82. In addition, the relative tube length increased to approximately 1.25 times (μm) in BSA-ICG-Cu(II) in comparison to control. Cu(II) is already known to promote angiogenesis by activating the HIF-1 pathway and here we observed that the performance of BSA-ICG-Cu(II) is better than BSA-Cu(II), which suggests that the improved angiogenesis is not only because of the mere presence of the Cu(II) in the system but the whole molecular complex has a role in activating the angiogenic pathway.

4. Conclusions

Here, we have categorically shown that an NIR-responsive multifunctional molecular platform can be developed by simply combining BSA, ICG, and Cu(II) by exploiting the binding affinity of ICG and Cu(II) to the BSA. Results revealed that the BSA-ICG-Cu(II) complex exhibited strong NIR emission, cytocompatibility, and appreciable photophysical properties. The NIR activation of the BSA-ICG-Cu(II) complex led to an increase in ROS generation with mild hyperthermia, which results in excellent bactericidal efficiency. When tested *in vitro* with dermal fibroblast and endothelial cells, we observed that the BSA-ICG-Cu(II) complex showed enhancement in cellular VEGF expression, dermal cell migration, and angiogenic properties. Interestingly, the therapeutic effect conferred by BSA-ICG)-Cu(II) was found to be synergistic with its constituents, which is very promising. This complex can be a good candidate for phototherapy-mediated chronic wound healing. However, it is important to mention that the results of the *in vitro* studies are only indicative of the therapeutic potential of the complex but the dose optimization and safety assessment needs to be determined precisely for further application to substantiate its potential. Furthermore, this NIR-

responsive platform has been developed to treat chronic wounds such as diabetic foot ulcers and is not a therapeutic solution to the underlying cause of the chronicity of the wound (such as diabetes in the case of diabetic foot ulcers). Therefore, for clinical success, the application of this complex should be aligned with the necessary systemic treatment. Addressing such concerns requires a comprehensive preclinical study of appropriate wound models, preferably in multidrug-resistant bacterial-infected diabetic wound models in rodents.

Data availability

The authors confirm that the data supporting the findings of this study are available within the article and its ESI materials.†

Author contributions

Indranil Banerjee: conceptualization, supervision, and writing – original draft. Jayashree Roy: formal analysis, investigation, and writing – original draft. Sahely Saha: investigation. Manjari Shukla: investigation. Raviraj Vankayala: review & editing. Sudipta Bhattacharyya: methodology. All the authors have approved the final version of the manuscript.

Conflicts of interest

The authors declare that there is no conflict of interest.

Acknowledgements

The authors would like to acknowledge the [i] grant received from SERB (CRG/2021/008145), [ii] facilities at the Duchenne Muscular Dystrophy (DMD) Research Centre at IIT Jodhpur, created through the IRPHA research grant scheme (IPA/2020/000015), funded by DST, SERB, [iii] the Centre for Research and Development of Scientific Instrumentation (CRDSI) Facility at the Indian Institute of Technology Jodhpur. The authors would also like to acknowledge Dr Vikash Chandra Janu, Defence Laboratory Jodhpur (DLJ), for extending research facilities. The authors would also like to thank the Ministry of Education (MoE), India, for providing financial support.

References

1 M. F. P. Graça, A. F. Moreira and I. J. Correia, Application of near-infrared light responsive biomaterials for improving the wound healing process: a review, *J. Drug Delivery Sci. Technol.*, 2024, **93**, 105409.
2 X. Wang, L. Qiu, C. Wang, Z. Gao, S. Zhou, P. Cui, P. Jiang, H. Hu, X. Ni, X. Du, J. Wang and J. Xia, Nanodot-doped peptide hydrogels for antibacterial phototherapy and wound healing, *Biomater. Sci.*, 2022, **10**, 654–664.
3 Y. Wang, Y. Jin, W. Chen, J. Wang, H. Chen, L. Sun, X. Li, J. Ji, Q. Yu, L. Shen and B. Wang, Construction of nanomaterials with targeting phototherapy properties to inhibit resistant bacteria and biofilm infections, *Chem. Eng. J.*, 2019, **358**, 74–90.
4 Y. Xu, H. Chen, Y. Fang and J. Wu, Hydrogel Combined with Phototherapy in Wound Healing, *Adv. Healthcare Mater.*, 2022, **11**(16), e2200494.
5 G. Wei, G. Yang, Y. Wang, H. Jiang, Y. Fu, G. Yue and R. Ju, Phototherapy-based combination strategies for bacterial infection treatment, *Theranostics*, 2020, **10**, 12241–12262.
6 B. Pucelik and J. M. Dąbrowski, Photodynamic inactivation (PDI) as a promising alternative to current pharmaceuticals for the treatment of resistant microorganisms, *Adv. Inorg. Chem.*, 2022, **79**, 65–108.
7 L. He, D. Di, X. Chu, X. Liu, Z. Wang, J. Lu, S. Wang and Q. Zhao, Photothermal antibacterial materials to promote wound healing, *J. Controlled Release*, 2023, **363**, 180–200.
8 I. Lee, J. Moon, H. Lee, S. Koh, G.-M. Kim, L. Gauthé, F. Stellacci, Y. S. Huh, P. Kim and D. C. Lee, Photodynamic treatment of multidrug-resistant bacterial infection using indium phosphide quantum dots, *Biomater. Sci.*, 2022, **10**, 7149–7161.
9 K. Bilici, N. Atac, A. Muti, I. Baylam, O. Dogan, A. Sennaroglu, F. Can and H. Yagci Acar, Broad spectrum antibacterial photodynamic and photothermal therapy achieved with indocyanine green loaded SPIONs under near infrared irradiation, *Biomater. Sci.*, 2020, **8**, 4616–4625.
10 X. Cai, J. Tian, J. Zhu, J. Chen, L. Li, C. Yang, J. Chen and D. Chen, Photodynamic and photothermal co-driven CO-enhanced multi-mode synergistic antibacterial nanoplatform to effectively fight against biofilm infections, *Chem. Eng. J.*, 2021, **426**, 131919.
11 J. Sun, L. Song, Y. Fan, L. Tian, S. Luan, S. Niu, L. Ren, W. Ming and J. Zhao, Synergistic Photodynamic and Photothermal Antibacterial Nanocomposite Membrane Triggered by Single NIR Light Source, *ACS Appl. Mater. Interfaces*, 2019, **11**, 26581–26589.
12 D. Vecchio, T. Dai, L. Huang, L. Fantetti, G. Roncucci and M. R. Hamblin, Antimicrobial photodynamic therapy with RLP068 kills methicillin-resistant *Staphylococcus aureus* and improves wound healing in a mouse model of infected skin abrasion PDT with RLP068/Cl in infected mouse skin abrasion, *J. Biophotonics*, 2013, **6**, 733–742.
13 X. Shen, L. Dong, X. He, C. Zhao, W. Zhang, X. Li and Y. Lu, Treatment of infected wounds with methylene blue photodynamic therapy: an effective and safe treatment method, *Photodiagn. Photodyn. Ther.*, 2020, **32**, 102051.
14 K. da Silva Souza Campanholi, R. Combuca da Silva Junior, I. Cazelatto da Silva, R. Said dos Santos, C. F. Vecchi, M. L. Bruschi, M. Soares dos Santos Pozza, L. Vizioli de Castro-Hoshino, M. L. Baesso, N. Hioka, W. Caetano and V. R. Batistela, Stimulus-responsive phototherapeutic micellar platform of Rose Bengal B: a new perspective for the treatment of wounds, *J. Drug Delivery Sci. Technol.*, 2021, **66**, 102739.
15 B. C. L. Chan, P. Dharmaratne, B. Wang, K. M. Lau, C. C. Lee, D. W. S. Cheung, J. Y. W. Chan, G. G. L. Yue, C. B. S. Lau, C. K. Wong, K. P. Fung and M. Ip, Hypericin and Pheophorbide a Mediated Photodynamic Therapy Fighting MRSA Wound Infections: A Translational Study from *In Vitro* to *In Vivo*, *Pharmaceutics*, 2021, **13**, 1399.

16 Z. Lu, T. Dai, L. Huang, D. B. Kurup, G. P. Tegos, A. Jahnke, T. Wharton and M. R. Hamblin, Photodynamic Therapy with A Cationic Functionalized Fullerene Rescues Mice From Fatal Wound Infections, *Nanomedicine*, 2010, **5**, 1525–1533.
17 Q. Gao, D. Huang, Y. Deng, W. Yu, Q. Jin, J. Ji and G. Fu, Chlorin e6 (Ce6)-loaded supramolecular polypeptide micelles with enhanced photodynamic therapy effect against *Pseudomonas aeruginosa*, *Chem. Eng. J.*, 2021, **417**, 129334.
18 Z. Wan, P. Zhang, L. Lv and Y. Zhou, NIR light-assisted phototherapies for bone-related diseases and bone tissue regeneration: a systematic review, *Theranostics*, 2020, **10**, 11837–11861.
19 H. U. Kim, T. Kim, C. Kim, M. Kim and T. Park, Recent Advances in Structural Design of Efficient Near-Infrared Light-Emitting Organic Small Molecules, *Adv. Funct. Mater.*, 2023, **33**, 2208082.
20 S. Golovynskyi, I. Golovynska, L. I. Stepanova, O. I. Datsenko, L. Liu, J. Qu and T. Y. Ohulchanskyy, Optical windows for head tissues in near-infrared and short-wave infrared regions: approaching transcranial light applications, *J. Biophotonics*, 2018, **11**(12), e201800141.
21 Y. Yang, J. Aw and B. Xing, Nanostructures for NIR light-controlled therapies, *Nanoscale*, 2017, **9**, 3698–3718.
22 B. Tao, C. Lin, A. Guo, Y. Yu, X. Qin, K. Li, H. Tian, W. Yi, D. Lei and L. Chen, Fabrication of copper ions-substituted hydroxyapatite/polydopamine nanocomposites with high antibacterial and angiogenesis effects for promoting infected wound healing, *J. Ind. Eng. Chem.*, 2021, **104**, 345–355.
23 Y. Fan, Z. Wang, W. Ren, G. Liu, J. Xing, T. Xiao, W. Li, Y. Li, P. Yu, C. Ning and Z. Song, Space-Confined Synthesis of Thin Polypyrrole Nanosheets in Layered Bismuth Oxychloride for a Photoresponse Antibacterial within the Near-Infrared Window and Accelerated Wound Healing, *ACS Appl. Mater. Interfaces*, 2022, **14**, 36966–36979.
24 X. Chu, P. Zhang, Y. Wang, B. Sun, Y. Liu, Q. Zhang, W. Feng, Z. Li, K. Li, N. Zhou and J. Shen, Near-infrared carbon dot-based platform for bioimaging and photothermal/photodynamic/quaternary ammonium triple synergistic sterilization triggered by single NIR light source, *Carbon N Y*, 2021, **176**, 126–138.
25 C. Shirata, J. Kaneko, Y. Inagaki, T. Kokudo, M. Sato, S. Kiritani, N. Akamatsu, J. Arita, Y. Sakamoto, K. Hasegawa and N. Kokudo, Near-infrared photothermal/photodynamic therapy with indocyanine green induces apoptosis of hepatocellular carcinoma cells through oxidative stress, *Sci. Rep.*, 2017, **7**(1), 1–8.
26 G. Zhu, B. Gao, J. Fan, J. Chen, S. Su, X. Yang, B. Li and C. Fang, ICG-mediated fluorescence-assisted debridement to promote wound healing, *PLoS One*, 2023, **18**, e0291508.
27 T.-W. Wong, S.-Z. Liao, W.-C. Ko, C.-J. Wu, S. B. Wu, Y.-C. Chuang and I.-H. Huang, Indocyanine Green—Mediated Photodynamic Therapy Reduces Methicillin-Resistant Staphylococcus aureus Drug Resistance, *J. Clin. Med.*, 2019, **8**, 411.
28 H. Qiu, S. Zhu, L. Pang, J. Ma, Y. Liu, L. Du, Y. Wu and Y. Jin, ICG-loaded photodynamic chitosan/polyvinyl alcohol composite nanofibers: Anti-resistant bacterial effect and improved healing of infected wounds, *Int. J. Pharm.*, 2020, **588**, 119797.
29 H. Wang, X. Li, B. W.-C. Tse, H. Yang, C. A. Thorling, Y. Liu, M. Touraud, J. B. Chouane, X. Liu, M. S. Roberts and X. Liang, Indocyanine green-incorporating nanoparticles for cancer theranostics, *Theranostics*, 2018, **8**, 1227–1242.
30 V. Saxena, M. Sadoqi and J. Shao, Degradation Kinetics of Indocyanine Green in Aqueous Solution, *J. Pharm. Sci.*, 2003, **92**, 2090–2097.
31 C. D. Geddes, H. Cao and J. R. Lakowicz, Enhanced photostability of ICG in close proximity to gold colloids, *Spectrochim. Acta, Part A*, 2003, **59**, 2611–2617.
32 Y. Xu, W. Zhou, L. Xiao, Q. Lan, M. Li, Y. Liu, L. Song and L. Li, Bacitracin-Engineered BSA/ICG Nanocomplex with Enhanced Photothermal and Photodynamic Antibacterial Activity, *ACS Omega*, 2022, **7**, 33821–33829.
33 J. Zhou, H. Wang, H. Wu, D. Lan, Y. Peng, Z. Li and F. Dai, Electrospun SF/PLGA/ICG Composite Nanofibrous Membranes for Potential Wound Healing and Tumor Therapy, *Processes*, 2022, **10**, 850.
34 S. Hui, Q. Liu, Y. Han, L. Zhang, J. Yang, S. Jiang, H. Qian and W. Yang, ICG@ZIF-8/PDA/Ag composites as chemo-photothermal antibacterial agents for efficient sterilization and enhanced wound disinfection, *J. Mater. Chem. B*, 2021, **9**, 9961–9970.
35 L. Li, G. Zhu, W. Xu, M. Wang, Y. Xie, Z. Bao, M. Qi, M. Gao and C. Li, Construction of mPt/ICG-αA nanoparticles with enhanced phototherapeutic activities for multidrug-resistant bacterial eradication and wound healing, *Nanoscale*, 2023, **15**, 13617–13627.
36 F. An, Z. Yang, M. Zheng, T. Mei, G. Deng, P. Guo, Y. Li and R. Sheng, Rationally assembled albumin/indocyanine green nanocomplex for enhanced tumor imaging to guide photothermal therapy, *J. Nanobiotechnol.*, 2020, **18**, 1–11.
37 F. Zhang, H. Yang, Y. Yang, H. Wang, X. Li and X. Wu, Stretchable and biocompatible bovine serum albumin fibrous films supported silver for accelerated bacteria-infected wound healing, *Chem. Eng. J.*, 2021, **417**, 129145.
38 D. Liu, S. Zhao, Y. Jiang, C. Gao, Y. Wu and Y. Liu, Biocompatible dual network bovine serum albumin-loaded hydrogel-accelerates wound healing, *Eur. Polym. J.*, 2023, **185**, 111820.
39 Y. Wang, J. Guo, B. Li, D. Li, Z. Meng and S.-K. Sun, Biocompatible therapeutic albumin/genipin bioglue for postoperative wound adhesion and residual tumor ablation, *Biomaterials*, 2021, **279**, 121179.
40 C. K. Sen, S. Khanna, M. Venojarvi, P. Trikha, E. Christopher Ellison, T. K. Hunt and S. Roy, Copper-induced vascular endothelial growth factor expression and wound healing, *Am. J. Physiol.: Heart Circ. Physiol.*, 2002, **282**, 1821–1827.
41 J. Li, D. Zhai, F. Lv, Q. Yu, H. Ma, J. Yin, Z. Yi, M. Liu, J. Chang and C. Wu, Preparation of copper-containing bioactive glass/eggshell membrane nanocomposites for improving angiogenesis, antibacterial activity and wound healing, *Acta Biomater.*, 2016, **36**, 254–266.

42 X. Wang, F. Cheng, J. Liu, J.-H. Smått, D. Gepperth, M. Lastusaari, C. Xu and L. Hupa, Biocomposites of copper-containing mesoporous bioactive glass and nanofibrillated cellulose: Biocompatibility and angiogenic promotion in chronic wound healing application, *Acta Biomater.*, 2016, **46**, 286–298.

43 N. M. O'Boyle, M. Banck, C. A. James, C. Morley, T. Vandermeersch and G. R. Hutchison, Open Babel: An open chemical toolbox, *J. Cheminf.*, 2011, **3**, 33.

44 A. Bujacz, Structures of bovine, equine and leporine serum albumin, *Acta Crystallogr., Sect. D:Biol. Crystallogr.*, 2012, **68**, 1278–1289.

45 G. M. Morris, R. Huey, W. Lindstrom, M. F. Sanner, R. K. Belew, D. S. Goodsell and A. J. Olson, AutoDock4 and AutoDockTools4: automated docking with selective receptor flexibility, *J. Comput. Chem.*, 2009, **30**, 2785–2791.

46 J. C. Phillips, D. J. Hardy, J. D. C. Maia, J. E. Stone, J. V. Ribeiro, R. C. Bernardi, R. Buch, G. Fiorin, J. Hénin, W. Jiang, R. McGreevy, M. C. R. Melo, B. K. Radak, R. D. Skeel, A. Singharoy, Y. Wang, B. Roux, A. Aksimentiev, Z. Luthey-Schulten, L. V. Kalé, K. Schulten, C. Chipot and E. Tajkhorshid, Scalable molecular dynamics on CPU and GPU architectures with NAMD, *J. Chem. Phys.*, 2020, **153**(4), 044130.

47 W. Humphrey, A. Dalke and K. Schulten, VMD: Visual molecular dynamics, *J. Mol. Graphics*, 1996, **14**, 33–38.

48 S. Kim, J. Lee, S. Jo, C. L. Brooks, H. S. Lee and W. Im, CHARMM-GUI ligand reader and modeler for CHARMM force field generation of small molecules, *J. Comput. Chem.*, 2017, **38**, 1879–1886.

49 M. Boyles, F. Murphy, W. Mueller, W. Wohlleben, N. R. Jacobsen, H. Braakhuis, A. Giusti and V. Stone, Development of a standard operating procedure for the DCFH$_2$-DA acellular assessment of reactive oxygen species produced by nanomaterials, *Toxicol. Mech. Methods*, 2022, **32**, 439–452.

50 J. Mérian, R. Boisgard, P.-A. Bayle, M. Bardet, B. Tavitian and I. Texier, Comparative biodistribution in mice of cyanine dyes loaded in lipid nanoparticles, *Eur. J. Pharm. Biopharm.*, 2015, **93**, 1–10.

51 V. E. Lee, J. M. Schulman, E. I. Stiefel and C. C. Lee, Reversible precipitation of bovine serum albumin by metal ions and synthesis, structure and reactivity of new tetrathiometallate chelating agents, *J. Inorg. Biochem.*, 2007, **101**, 1707–1718.

52 R. John, J. Mathew, A. Mathew, C. T. Aravindakumar and U. K. Aravind, Probing the Role of Cu(II) Ions on Protein Aggregation Using Two Model Proteins, *ACS Omega*, 2021, **6**, 35559–35571.

53 Y. Q. Wang, H. M. Zhang, G. C. Zhang, W. H. Tao, Z. H. Fei and Z. T. Liu, Spectroscopic studies on the interaction between silicotungstic acid and bovine serum albumin, *J. Pharm. Biomed. Anal.*, 2007, **43**, 1869–1875.

54 B. Lemli, D. Derdák, P. Laczay, D. Kovács and S. Kunsági-Máté, Noncovalent Interaction of Tilmicosin with Bovine Serum Albumin, *Molecules*, 2018, **23**, 1915.

55 S. Cao, B. Liu, Z. Li and B. Chong, A fluorescence spectroscopic study of the interaction between Glipizide and bovine serum albumin and its analytical application, *J. Lumin.*, 2014, **145**, 94–99.

56 G. Li, B. S. Liu, Q. Zhang and R. Han, Investigation on the effect of fluorescence quenching of bovine serum albumin by cefoxitin sodium using fluorescence spectroscopy and synchronous fluorescence spectroscopy, *Luminescence*, 2016, **31**, 1054–1062.

57 J. Cho, F. Nouizi, C.-S. Kim and G. Gulsen, Monitoring Distribution of the Therapeutic Agent Dimethyl Sulfoxide *via* Solvatochromic Shift of Albumin-Bound Indocyanine Green, *Sensors*, 2023, **23**, 7728.

58 S. Paul, N. Sepay, S. Sarkar, P. Roy, S. Dasgupta, P. Saha Sardar and A. Majhi, Interaction of serum albumins with fluorescent ligand 4-azido coumarin: spectroscopic analysis and molecular docking studies, *New J. Chem.*, 2017, **41**, 15392–15404.

59 N. Tayeh, T. Rungassamy and J. R. Albani, Fluorescence spectral resolution of tryptophan residues in bovine and human serum albumins, *J. Pharm. Biomed. Anal.*, 2009, **50**, 107–116.

60 N. Shahabadi, M. Maghsudi and S. Rouhani, Study on the interaction of food colourant quinoline yellow with bovine serum albumin by spectroscopic techniques, *Food Chem.*, 2012, **135**, 1836–1841.

61 M. Bhattacharya, N. Jain, K. Bhasne, V. Kumari and S. Mukhopadhyay, pH-induced Conformational Isomerization of Bovine Serum Albumin Studied by Extrinsic and Intrinsic Protein Fluorescence, *J. Fluoresc.*, 2011, **21**, 1083–1090.

62 C. Ota, S. Tanaka and K. Takano, Revisiting the Rate-Limiting Step of the ANS–Protein Binding at the Protein Surface and Inside the Hydrophobic Cavity, *Molecules*, 2021, **26**, 420.

63 Y. Prince, N. Hiremath and R. Vankayala, Near-infrared light activatable niosomes loaded with indocyanine green and plasmonic gold nanorods for theranostic applications, *Biomater. Sci.*, 2023, **11**, 7759–7767.

64 H. Kida, Y. Yamasaki, L. B. Feril Jr, H. Endo, K. Itaka and K. Tachibana, Efficient mRNA Delivery with Lyophilized Human Serum Albumin-Based Nanobubbles, *Nanomaterials*, 2023, **13**, 1283.

65 S. Tayyab and S. R. Feroz, Serum albumin: clinical significance of drug binding and development as drug delivery vehicle, *Adv. Protein Chem. Struct. Biol.*, 2021, **123**, 193–218.

66 K. M. K. Sand, M. Bern, J. Nilsen, H. T. Noordzij, I. Sandlie and J. T. Andersen, Unraveling the Interaction between FcRn and Albumin: Opportunities for Design of Albumin-Based Therapeutics, *Front. Immunol.*, 2015, **5**, 682.

67 W. Bal, J. Christodoulou, P. J. Sadler and A. Tucker, Multi-metal binding site of serum albumin, *J. Inorg. Biochem.*, 1998, **70**, 33–39.

68 W. Bal, M. Sokołowska, E. Kurowska and P. Faller, Binding of transition metal ions to albumin: Sites, affinities and rates, *Biochim. Biophys. Acta, Gen. Subj.*, 2013, **1830**, 5444–5455.

69 C. Li, X. He, Q. Li, M. Lv, J. Shen, L. Jin and D. He, A photothermal-response oxygen release platform based on

a hydrogel for accelerating wound healing, *NPG Asia Mater.*, 2023, **15**, 3.

70 X. Dong, J. Ye, Y. Chen, T. Tanziela, H. Jiang and X. Wang, Intelligent peptide-nanorods against drug-resistant bacterial infection and promote wound healing by mild-temperature photothermal therapy, *Chem. Eng. J.*, 2022, **432**, 134061.

71 S. L. Percival, I. Francolini and G. Donelli, Low-level Laser Therapy as an Antimicrobial and Antibiofilm Technology and its Relevance to Wound Healing, *Future Microbiol.*, 2015, **10**, 255–272.

72 Y. Xiao, J. Peng, Q. Liu, L. Chen, K. Shi, R. Han, Q. Yang, L. Zhong, R. Zha, Y. Qu and Z. Qian, Ultrasmall CuS@BSA nanoparticles with mild photothermal conversion synergistically induce MSCs-differentiated fibroblast and improve skin regeneration, *Theranostics*, 2020, **10**, 1500–1513.

73 M. Boyles, F. Murphy, W. Mueller, W. Wohlleben, N. R. Jacobsen, H. Braakhuis, A. Giusti and V. Stone, Development of a standard operating procedure for the DCFH $_2$ -DA acellular assessment of reactive oxygen species produced by nanomaterials, *Toxicol. Mech. Methods*, 2022, **32**, 439–452.

74 K. Bilici, N. Atac, A. Muti, I. Baylam, O. Dogan, A. Sennaroglu, F. Can and H. Yagci Acar, Broad spectrum antibacterial photodynamic and photothermal therapy achieved with indocyanine green loaded SPIONs under near infrared irradiation, *Biomater. Sci.*, 2020, **8**, 4616–4625.

75 H. Qiu, S. Zhu, L. Pang, J. Ma, Y. Liu, L. Du, Y. Wu and Y. Jin, ICG-loaded photodynamic chitosan/polyvinyl alcohol composite nanofibers: Anti-resistant bacterial effect and improved healing of infected wounds, *Int. J. Pharm.*, 2020, **588**, 119797.

76 P.-Y. Xu, R. K. Kankala, Y.-W. Li, S.-B. Wang and A.-Z. Chen, Synergistic chemo-/photothermal therapy based on supercritical technology-assisted chitosan–indocyanine green/luteolin nanocomposites for wound healing, *Regener. Biomater.*, 2024, **11**, rbae037.

77 X. Yi, Q.-Y. Duan and F.-G. Wu, Low-Temperature Photothermal Therapy: Strategies and Applications, *Research*, 2021, **2021**, DOI: **10.34133/2021/9816594**.

78 X. Zhang, B. Tan, Y. Wu, M. Zhang and J. Liao, A Review on Hydrogels with Photothermal Effect in Wound Healing and Bone Tissue Engineering, *Polymers*, 2021, **13**, 2100.

79 L. Sheng, Z. Zhang, Y. Zhang, E. Wang, B. Ma, Q. Xu, L. Ma, M. Zhang, G. Pei and J. Chang, A novel "hot spring"-mimetic hydrogel with excellent angiogenic properties for chronic wound healing, *Biomaterials*, 2021, **264**, 120414.

80 L. Miao, Z. Xu, J. Sui, X. Meng, S. Huo, S. Liu, M. Chen, Z. Zheng, X. Cai and H. Zhang, A New Nanoplatform Under NIR Released ROS Enhanced Photodynamic Therapy and Low Temperature Photothermal Therapy for Antibacterial and Wound Repair, *Int. J. Nanomed.*, 2024, **19**, 7509–7527.

81 Y. Xu, W. Zhou, L. Xiao, Q. Lan, M. Li, Y. Liu, L. Song and L. Li, Bacitracin-Engineered BSA/ICG Nanocomplex with Enhanced Photothermal and Photodynamic Antibacterial Activity, *ACS Omega*, 2022, **7**, 33821–33829.

82 M. Sun, P. Gao, B. Wang, X. Li, D. Shao, Y. Xu, L. Li, Y. Li, J. Zhu, W. Li and Y. Xue, Polydopamine-functionalized selenium nanoparticles as an efficient photoresponsive antibacterial platform, *RSC Adv.*, 2023, **13**, 9998–10004.

83 Z. Bahouth, B. Moskovitz, S. Halachmi and O. Nativ, Bovine serum albumin–glutaraldehyde (BioGlue®) tissue adhesive *versus* standard renorrhaphy following renal mass enucleation: a retrospective comparison, *Adv. Urol.*, 2017, **9**, 67–72.

84 G. Borkow, Using Copper to Improve the Well-Being of the Skin, *Curr. Chem. Biol.*, 2015, **8**, 89–102.

85 J. Xiao, S. Chen, J. Yi, H. F. Zhang and G. A. Ameer, A Cooperative Copper Metal–Organic Framework-Hydrogel System Improves Wound Healing in Diabetes, *Adv. Funct. Mater.*, 2017, **27**(1), 1604872.

86 Z. Zhang, H. Xue, Y. Xiong, Y. Geng, A. C. Panayi, S. Knoedler, G. Dai, M.-A. Shahbazi, B. Mi and G. Liu, Copper incorporated biomaterial-based technologies for multifunctional wound repair, *Theranostics*, 2024, **14**, 547–570.

87 S. Chung, A. K. Roy and T. J. Webster, Selenium Nanoparticle Protection of Fibroblast Stress: Activation of ATF4 and Bcl-xL Expression, *Int. J. Nanomed.*, 2019, **14**, 9995–10007.

88 L. E. Tracy, R. A. Minasian and E. J. Caterson, Extracellular Matrix and Dermal Fibroblast Function in the Healing Wound, *Adv. Wound Care*, 2016, **5**, 119–136.

89 M. N. M. Walter, K. T. Wright, H. R. Fuller, S. MacNeil and W. E. B. Johnson, Mesenchymal stem cell-conditioned medium accelerates skin wound healing: An *in vitro* study of fibroblast and keratinocyte scratch assays, *Exp. Cell Res.*, 2010, **316**, 1271–1281.

90 M. Shibuya, Vascular Endothelial Growth Factor (VEGF) and Its Receptor (VEGFR) Signaling in Angiogenesis: A Crucial Target for Anti- and Pro-Angiogenic Therapies, *Genes Cancer*, 2011, **2**, 1097–1105.

91 F. Shams, H. Moravvej, S. Hosseinzadeh, E. Mostafavi, H. Bayat, B. Kazemi, M. Bandehpour, E. Rostami, A. Rahimpour and H. Moosavian, Overexpression of VEGF in dermal fibroblast cells accelerates the angiogenesis and wound healing function: *in vitro* and *in vivo* studies, *Sci. Rep.*, 2022, **12**, 18529.

92 Z. Zhang, H. Xue, Y. Xiong, Y. Geng, A. C. Panayi, S. Knoedler, G. Dai, M.-A. Shahbazi, B. Mi and G. Liu, Copper incorporated biomaterial-based technologies for multifunctional wound repair, *Theranostics*, 2024, **14**, 547–570.

93 W. Feng, F. Ye, W. Xue, Z. Zhou and Y. J. Kang, Copper Regulation of Hypoxia-Inducible Factor-1 Activity, *Mol. Pharmacol.*, 2009, **75**, 174–182.

94 M. G. Tonnesen, X. Feng and R. A. F. Clark, Angiogenesis in Wound Healing, *J. Invest. Dermatol. Symp. Proc.*, 2000, **5**, 40–46.